Dynamic passive control of turbulent drag via subsurface resonant phononic material

Ching-Te Lin *[1], Vinod Ramakrishnan †[2], Andres Goza ‡[2], Kathryn H. Matlack §[2], and H. Jane Bae ¶[1]
[1]*California Institute of Technology, Pasadena, CA, 91125, USA*
[2]*University of Illinois at Urbana-Champaign, Urbana, Illinois, 6180, USA*

This work presents a passive turbulence-control strategy based on a resonant phononic material (RPM) embedded beneath the surface of a turbulent channel flow. The RPM is modeled as a mass–spring–damper chain tuned to a defect-induced resonance that interacts with near-wall turbulence. Using a weakly coupled fluid–metamaterial framework, we show that both the wall-pressure forcing and the RPM response collapse onto a narrow frequency band dictated by the designed resonance, and that within a moderate actuation-amplitude range the system produces measurable transient drag-reduction effects. Direct numerical simulations (DNS) further reveal a well-defined stable interval of RPM damping coefficients, with a sharp transition between underdamped (growing) and overdamped (bounded) response regimes. To enable rapid exploration of RPM configurations, we also develop a reduced-order weakly coupled model in which a linear wall-pressure approximation replaces the full pressure-Poisson solution; this simplified model accurately reproduces the key bifurcation behavior observed in DNS. Overall, the study clarifies the mechanisms governing RPM–flow coupling and informs the design of passive, energy-efficient compliant surfaces for aerodynamic applications.

I. Introduction

Turbulent drag constitutes a significant portion of energy consumption across many industrial sectors. For example, commercial aircraft expend nearly half of their total energy to overcome turbulent skin friction [1], and turbulent drag similarly dominates the energy required for long-distance fluid transport in pipelines. Consequently, even modest reductions in drag can yield substantial savings in energy and operational costs. Numerous passive surface-modification strategies have been proposed over the past several decades, but these approaches typically rely on static geometries or simple dynamic responses, limiting their applicability across varying operating conditions.

The emergence of phononic materials, engineered media with spatially periodic and architected internal structure, offers an opportunity to expand the scope of passive turbulent flow control. These materials can be tailored to achieve elasto-dynamic functionalities such as wave filtering[2] and guiding[3], directional energy propagation[4, 5], shape morphing[6]. Recent advances even allow post-fabrication tuning of phononic architectures [7], a capability well aligned with flow-control applications where dominant frequencies and operating conditions (e.g., speed and altitude in aerial vehicle operations, internal fluid and external ambient temperature in industrial fluid pipelines).

In this study, we explore the interaction between a turbulent channel flow and a phononic material embedded beneath the wall surface. The phononic material is designed to possess an eigenmode that aligns with the dominant flow frequencies, and the wall is embedded with multiple panels of phononic materials spaced according to the primary turbulent wavelengths identified in our previous active-control studies[8]. Embedding phononic materials beneath the wall surface enables a dynamic passive control mechanism, where the system requires no external actuation, yet the compliant subsurface can deform in response to flow forcing in a manner reminiscent of active control strategies.

Two primary pathways for passive drag reduction have historically been considered. The first targets laminar–turbulent transition. Early work by Kramer [9–11] introduced the concept of compliant surfaces, which were subsequently validated by stability analyses [12–15] and direct numerical simulations [16, 17]. More recently, Hussein et al. [18] introduced the phononic subsurface (PSub), demonstrating that an elastic, architected interface can interact with Tollmien–Schlichting (TS) waves to modify perturbation kinetic-energy production. Subsequently, Barnes et al. [19]

*Graduate Student, Department of Mechanical and Civil Engineering, Student Member AIAA
†Postdoctoral Researcher, The Grainger College of Engineering, Department of Mechanical Science and Engineering
‡Assistant Professor, The Grainger College of Engineering, Department of Aerospace Engineering, Senior Member AIAA
§Associate Professor, The Grainger College of Engineering, Department of Mechanical Science and Engineering
¶Assistant Professor, Graduate Aerospace Laboratories, Senior Member AIAA

conducted an initial computational investigation showing that a beam-based PSub embedded within a flat plate boundary layer can exhibit out-of-phase surface motion with respect to Tollmien–Schlichting (T–S) wave forcing, leading to local attenuation of perturbation kinetic energy. Building on this concept, Willey et al. [20] demonstrated that multi-input, multi-output (MIMO) PSubs allow passive realization of favorable phase relationships between surface displacement and external disturbances, enabling a degree of transition delay without active input.

The second pathway aims to modify fully developed turbulent boundary layers. Foundational work by Bushnell et al. [21] and subsequent theoretical analyses [22, 23] established the potential for compliant surfaces to interact resonantly with turbulent motions. Early demonstrations showed drag reductions on the order of 7% in low-Reynolds-number channel flows [24], with later studies exploring anisotropic designs [25], shear-driven wall models [26], and space–time compliant-surface dynamics [27]. Luhar et al. [28] provided a resolvent-based framework for analyzing these effects. Despite these advances, achieving consistent, robust, and passive drag reduction in turbulent regimes remains elusive.

The demonstrated success of phononic materials in transition delay suggests an untapped potential for their use in turbulent drag reduction. Motivated by this opportunity, we investigate the coupled dynamics of resonant phononic materials interacting with turbulent wall-bounded flows. Our objective is to design phononic materials with resonant properties that match those of dominant turbulent flow coherences (here we avoid the term "structures" to prevent confusion with the material structure). By doing so, we aim to characterize how phononic resonances can passively influence the near-wall turbulence with minimal energy input.

To this end, we conduct high-fidelity simulations of channel flow weakly coupled to an resonant phononic material subsurface via a blowing–suction boundary condition at a fixed wall location. This velocity-based weak coupling is appropriate in the small-displacement limit and serves as a starting point for future strongly coupled studies involving moving boundaries. Consistent with the small amplitude assumption, we focus on cases where the oscillating velocity amplitude, $A^+ \leq 0.7$, where the superscript + indicates viscous units defined by the fluid kinematic viscosity ν and friction velocity u_τ.

This paper is organized as follows. In section II, we propose a novel fluid–metamaterial interaction (FMI) control framework for wall-bounded turbulence using a resonant phononic material (RPM) embedded beneath the wall. As described in Section II, we design the structural parameters based on open-loop flow characteristics[8] to minimize the turbulent drag. In Section III, we demonstrate through weakly coupled simulations that the RPM surface response exhibits bifurcation phenomenon among various damping coefficients in the resonant phononic material and achieves transient drag reduction with favourable oscillating amplitude. These results reveal key physical mechanisms by which compliant subsurfaces can passively shape turbulent dynamics. A broader discussion of the implications and future directions for sustainable control design is provided in Section IV.

II. Methodology

We investigate a novel passive flow control strategy based on resonant phononic materials (RPMs) integrated beneath the wall of a turbulent channel flow. The turbulent channel flow is driven at constant mass flow rate to achieve a friction Reynolds number $Re_\tau = u_\tau h/\nu \approx 180$, where h denotes the channel half-height. This corresponds to a bulk Reynolds number of $Re_b = U_b h/\nu \approx 2953$. Here, x_1, x_2, and x_3 denote the streamwise, wall-normal, and spanwise directions, respectively, and u_1, u_2, and u_3 denote the streamwise, wall-normal, and spanwise velocity components, respectively.

To interface with the turbulent flow, a subsurface composed of engineered phononic structures is embedded beneath the bottom wall. These structures are designed to selectively resonate at targeted frequencies and wavelengths. These frequency-wavelength pairs are selected to match those that yielded maximal drag reduction with *prescribed* blowing and suction, performed in a prior study[8].

A. FMI configuration

1. Turbulent Channel Flow-RPM Interaction Configuration

In this study, we adopt the small-displacement approximation, under which the wall deformation velocity can be approximated by an equivalent blowing and suction at the wall. The numerical coupling scheme is weakly-coupled, *i.e.*, the wall-normal velocity associated with RPM motion at current time step is computed based on the wall-normal force along the wall surface at previous time step.

The spatial placement of RPMs is based on prior works on actively oscillating surfaces. Specifically, Quadrio et al. [29] study the effect of steady blowing and suction on a turbulent channel flow under $Re_\tau \approx 180$. They pointed out that the streamwise-periodic blowing and suction can lead to drag reduction at moderate streamwise wavelength

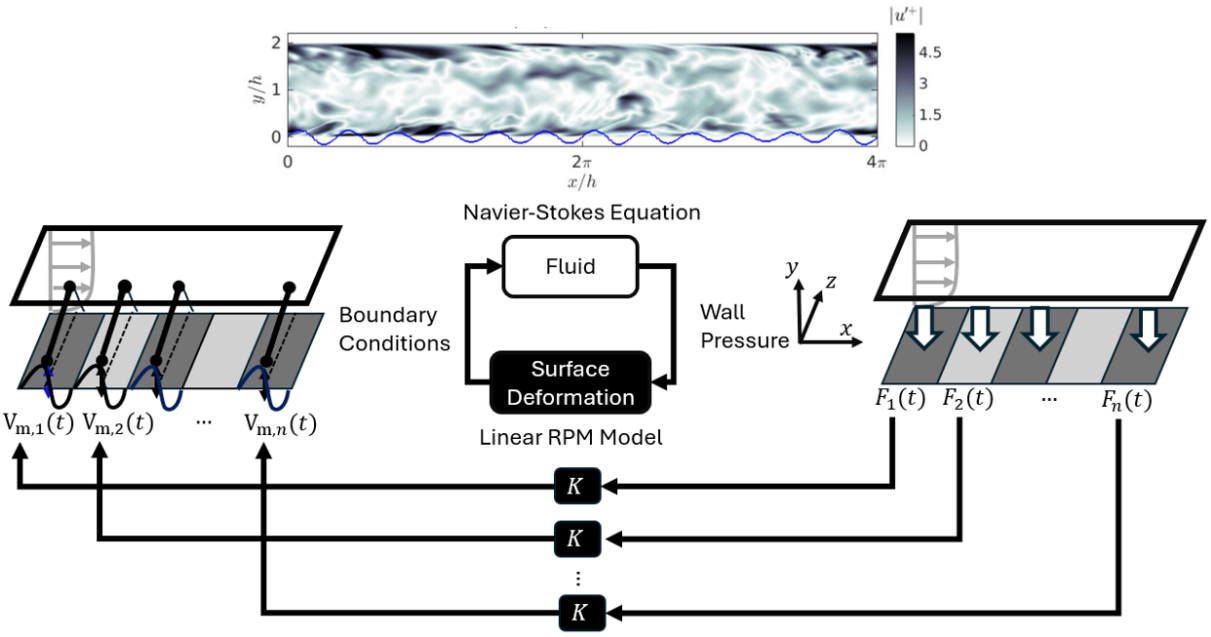

Fig. 1 Schematic graph of weakly-coupled simulation

($\lambda_1^+ \approx 206$). Lin et al. [8] further explored the time-varying blowing and suction. In their parametric study, they showed that the oscillating frequency ω^+ around 0.1 results in roughly 3% drag reduction. From the results of the prescribed motion study above, the optimal streamwise wavelength, λ_1^*, and frequency, ω^*, for an unsteady streamwise-periodic blowing and suction profile is given by $\lambda_1^{*+} \approx 206$ and $\omega^{*+} \approx 0.11$. Based on these findings, we adopt the bottom wall dynamics to be defined by pressure-driven RPM subsurfaces periodically placed in the streamwise direction, with each RPM oscillating in the wall-normal direction, as illustrated in Fig. 1. Each spanwise-aligned RPM segment is referred to as control panel from hereon. Each control panel consists of a designed RPM subsurface model, which deforms independently in the wall-normal direction, in response to the normal component of the force integrated along that entire panel. The streamwise length of each panel segment, $L_{1,p}$, is set close to the optimal wavelength identified in the harmonic forcing experiments, *i.e.*, $L_{1,p}^+ = \lambda_1^{*+} = 195$.

The RPM subsurface and turbulent channel flow are coupled through a weakly-coupled scheme. That is, at each time step, the fluid-induced load is applied as an averaged pressure force, F_w, calculated from the flow field (see section II.B) on the given RPM panel surface. Subsequently, the RPM surface velocity response, V_m, to the fluid loading is calculated and a weak fluid-RPM coupling is enforced by applying a RPM-informed blowing and suction boundary condition (Eq. (2)) at the bottom wall ($x_2 = 0$) for the next time step. This procedure is performed for each time step, simulating the weakly-coupled FSI dynamics for the total computational time.

2. RPM design

We choose a defect-embedded grounded monoatomic phononic crystal (PnC)[30] as the subsurface RPM model. PnCs are architected materials that can customize wave propagation by leveraging their structural periodicity. For a plane wave, $y(x,t) = \widetilde{y}\exp(\mathrm{i}(\kappa x - \omega t))$, where $\mathrm{i} = \sqrt{-1}$, traveling in a (defect-free) grounded monoatomic PnC with mass, m, and stiffness, k, the wavenumber-frequency ($\kappa - \omega$) dispersion relations[30] describing the wave characteristics feature two distinct regions[31]. The first region is the pass band (PB), where each temporal frequency ω is mapped onto a real spatial wavenumber, κ_R. This behavioral regime is marked by wave propagation into the material bulk. A second behavioral regime is the band gap (BG), where each ω is mapped onto a complex wavenumber, $\mathrm{i}\kappa_\mathrm{I}$ or $\pi + \mathrm{i}\kappa_\mathrm{I}$, leading to spatial attenuation of plane waves and no propagation into the material bulk.

The PB (solid) and BG (dashed) curves in Fig. 2 indicate the dispersion relations for an infinite (defect-free) grounded monoatomic PnC. The eigenfrequencies, $\omega_j \; \forall \; j = 1, 2, \ldots, N$, of a finite PnC lie on the κ_R curve where $\kappa_{\mathrm{R},j} = (j-1)\pi/(N-1)$. However, when we introduce a structural defect by breaking the periodicity of material

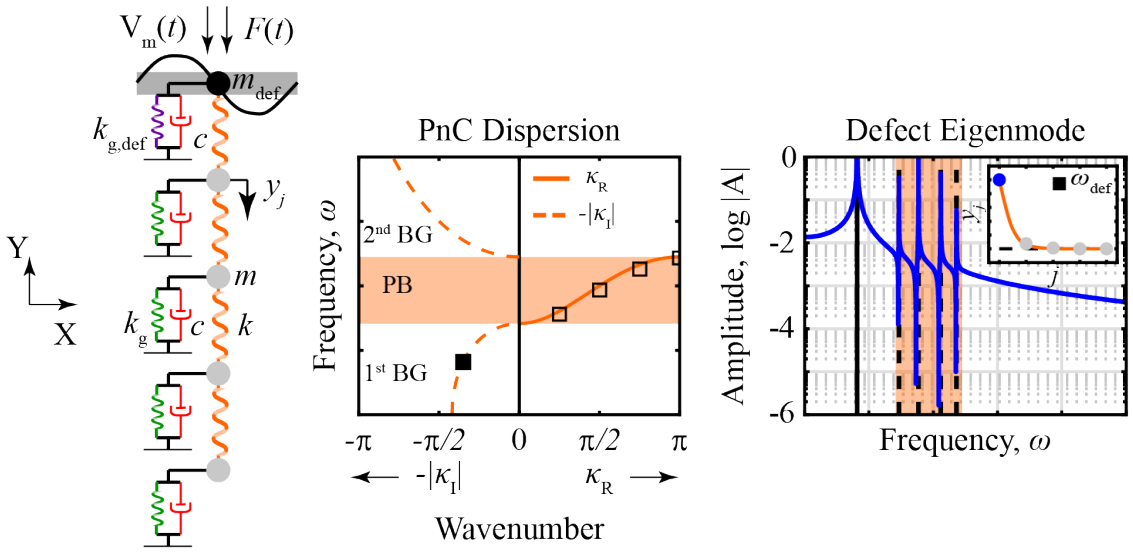

Fig. 2 RPM mass-spring-damper model, grounded monoatomic PnC dispersion curves with eigenvalues of the finite defect-embedded PnC overlayed, the fourier response function (FRF) calculated at the defect mass location, and the corresponding localized defect eigenmode (inset).

properties at one edge of the grounded monoatomic PnC, we can create an isolated resonance with a highly localized eigenmode shape within the PnC BG, as shown in Fig. 2. The PnC BG surrounding this defect resonance provides beneficial RPM responses to the broadband turbulent flow, e.g., spatial attenuation of other BG excitation frequencies leading to a narrow-band response centered at the defect frequency, ω_{def}, high energy localization at the fluid-RPM interface, stable pressure-deformation phase[18], motivating the choice of the defect-embedded grounded monoatomic PnC to interface with the stochastic and broadband turbulent channel flow. The matrix equations of motion of the RPM are given as

$$\tilde{\mathbf{M}}\ddot{\tilde{y}} + \tilde{\mathbf{C}}\dot{\tilde{y}} + \tilde{\mathbf{K}}\tilde{y} = \tilde{F}, \tag{1}$$

where $\tilde{y} = [\tilde{y}_1, \tilde{y}_2, \cdots, \tilde{y}_N]^{\mathrm{T}}$ represents the wall-normal displacement vector of an RPM with N masses, $\tilde{F}$, represents the fluid surface force, and

$$\tilde{\mathbf{M}} = \begin{bmatrix} \tilde{m}_{\text{def}} & 0 & \cdots & \cdots & 0 \\ 0 & \tilde{m} & \cdots & \cdots & 0 \\ \vdots & \vdots & \ddots & & \vdots \\ \vdots & \vdots & & \ddots & \vdots \\ 0 & 0 & \cdots & \cdots & \tilde{m} \end{bmatrix}_{\mathrm{N\times N}}, \tilde{\mathbf{C}} = \tilde{c}\mathbf{I}_{\mathrm{N\times N}}, \tilde{\mathbf{K}} = \begin{bmatrix} \tilde{k} + \tilde{k}_{\mathrm{g,def}} & -\tilde{k} & 0 & \cdots & 0 \\ -\tilde{k} & 2\tilde{k} + \tilde{k}_{\mathrm{g}} & -\tilde{k} & \cdots & 0 \\ 0 & -\tilde{k} & \ddots & & \vdots \\ \vdots & \vdots & & \ddots & -\tilde{k} \\ 0 & 0 & \cdots & -\tilde{k} & \tilde{k} + \tilde{k}_{\mathrm{g}} \end{bmatrix}_{\mathrm{N\times N}},$$

represent the mass, $\tilde{\mathbf{M}}$, damping, $\tilde{\mathbf{C}}$, and the stiffness, $\tilde{\mathbf{K}}$ matrices normalized in outer units, such that

$$\tilde{m} = \frac{m}{\rho h^3}, \quad \tilde{c} = \frac{c}{\rho U_b h^2}, \quad \tilde{k} = \frac{k}{\rho U_b^2 h}, \quad \tilde{F} = \frac{F}{\rho U_b^2 h^2}.$$

Here, U_b is the bulk velocity, and parameters $\{\tilde{m}, \tilde{c}, \tilde{k}, \tilde{k}_{\mathrm{g}}\}$ represent the periodic mass, damping, interaction and grounding stiffness properties of a grounded monoatomic PnC. Note that the undamped (i.e., $\tilde{c} = 0$) velocity response of the defect mass to a harmonic sinusoidal force of unit magnitude at resonant frequency, $F_1 = \sin(\omega_j t)$, becomes linearly unbounded: $\dot{\tilde{y}}_1 = \mathrm{A_E} t \sin(\omega_j t)$, where the amplitude envelope, $\mathrm{A_E}$, quantifies the linear rate of increase in velocity amplitude over time. The amplitude envelope is an important RPM behvaioral parameter that will determine the dynamic response ampltiude of the RPM in the FSI simulations. In addition, both the defect resonance frequency, $\omega_1 = \omega_{\text{def}}$, and the amplitude envelope, $\mathrm{A_E}$, are functions of the mass and stiffness properties of the RPM. Therefore, we alter these properties (i.e., $\{\tilde{m}_{\text{def}}, \tilde{k}_{\mathrm{g,def}}\}$) to precisely engineer a defect resonance, associated with the desired amplitude envelope, in the acoustic band gap, conducive for effective FSI.

Ensuring sufficient BG width around the target flow frequency, $\omega^{*+} \approx 0.11$, a desired exponentially decaying defect mode shape, we fix $\tilde{m} = 1, \tilde{k} = 0.826, \tilde{k}_g = 20.65$ for all our numerical studies, and leverage insights from previous studies[8] on turbulent flow control via unsteady wall-normal blowing and suction, to extract the conducive frequency, ω_{def}, and surface velocity, $V_m(t)(= \dot{y}_1)$, and choose appropriate defect material parameters, $\{\tilde{m}_{\text{def}}, \tilde{k}_{\text{g,def}}\}$ (see Tab. 1). Each RPM configuration in Tab. 1 is identified using the notation C#A#, where the numerical indices following "C" and "A" respectively denote the damping coefficient and amplitude envelope test cases of the RPM model. Configurations sharing the same C index correspond to cases with the same damping coefficient, while those sharing the same A index correspond to cases with the same amplitude envelope. The C index increases from low to high damping, and the A index increases from low to high amplitude envelope.

To simulate the deformation of RPM-based subsurface, the deformation is approximated via zeros-flux blowing and suction boundary condition. To ensure no-flux boundary condition at all times and replicating the harmonic surface velocity profile in prior prescribed studies[8], the spatial blowing and suction profile on j^{th} RPM panel is defined as a sinusoidal function in terms of the velocity of the defect chain's interface mass

$$u_2|_{x_2=0}(x_1, t) = V_m(t) \sin\left(\frac{2\pi x_1}{L_{1,p}}\right), \quad x_1 \in \left[(j-1)L_{1,p}, jL_{1,p}\right] \tag{2}$$

Table 1 Non-dimensional parameters for different RPM configurations. Reference values: $\tilde{m} = 1, \tilde{k} = 0.826, \tilde{k}_g = 20.65$.

ID	$\tilde{m}_{\text{def}}$	$\tilde{k}_{\text{g,def}}$	$\tilde{c}$
C1A4	1.84	1.19	0.37
C2A4	1.84	1.19	0.48
C3A4	1.84	1.19	0.51
C4A4	1.84	1.19	0.55
C3A1	7.37	7.16	0.51
C3A2	3.68	3.18	0.51
C3A3	2.45	1.85	0.51

B. Flow simulation setup

A series of direct numerical simulations (DNS) is conducted to evaluate the control performance of RPM panels integrated into a wall-bounded turbulent flow. The simulations solve the incompressible Navier–Stokes equations and the RPM equations of motion (Eq. (1)), simultaneously. Periodic boundary conditions are applied at the streamwise and spanwise boundaries, and a no-slip boundary condition is enforced on the top and bottom walls respectively for streamwise and spanwise velocity. Wall-normal velocity u_2 at the wall is determined via weakly-coupled scheme shown in prior section.

The computational domain (illustrated in the Fig. 1) has streamwise and spanwise lengths of $L_1/h = 4\pi$ and $L_3/h = 2\pi$, respectively. This domain size is determined through a series of numerical experiments in a prior study [8], which confirms that the minimal domain size required to study the effect of blowing and suction on the wall-shear stress is given by $(L_1/h, L_3/h) = (4\pi, 2\pi)$, corresponding to a computational domain that accommodates 12 control panels. Grid resolutions in the homogeneous streamwise and spanwise direction are uniform with $\Delta_1^+ \approx 9.97$ and $\Delta_3^+ \approx 4.98$, respectively. For the wall-normal direction, the grid is stretched using a hyperbolic tangent function such that Δ_2^+ varies from a minimum of 0.16 near the wall to a maximum of 7.34 at the channel center. The simulations utilize a staggered, second-order finite difference scheme [32] in space.

The time-marching scheme is given by the fractional-step method [33] with a third-order Runge–Kutta integration [34]. A fixed time step of $\Delta t^+ \approx 0.01$ is applied, and the total integration time is $T^+ \approx 4000$ to mitigate transient effects from additional periodic forcing. Code validation is achieved in prior studies of turbulent channel flow [35–37].

The averaged pressure force is obtained from the spatial-integrated wall pressure along the control panel. The pressure field p can be decomposed into imposed mean pressure gradient $\bar{p}$ and pressure fluctuation p'. The imposed

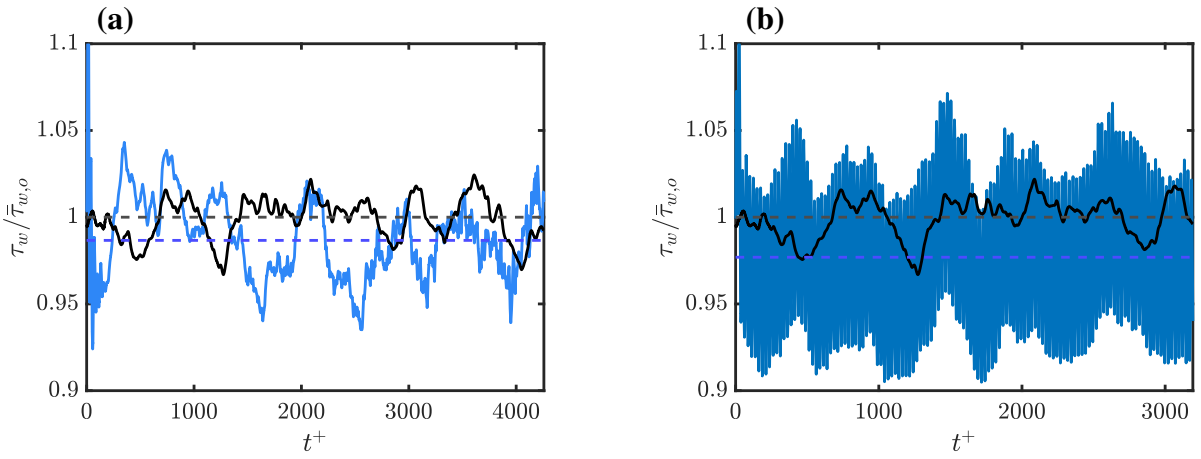

Fig. 3 Relative wall shear stress $\tau_w/\bar{\tau}_{w,o}$ for the controlled case (blue) and uncontrolled flow (black) for passive control with C2A4 (a) and prescribed control with $(A^+, \lambda_1^+, \omega^+) = (0.45, 180, 0.12)$ (b). Dashed blue line denote time-averaged values after transient state, $\langle \tau_w/\bar{\tau}_{w,o} \rangle = 98.6$ (a) and $\langle \tau_w/\bar{\tau}_{w,o} \rangle = 97.9$ (b). Dashed black line is $\tau_w/\bar{\tau}_{w,o} = 1$.

mean pressure gradient $\bar{p}$ is computed to maintain the constant mass flow rate, while the pressure fluctuation is computed via the pressure Poisson equation. In this study, we adopt the simplified form of the pressure Poisson equation used in the previous unsteady wall-transpiration case by Toedtli et al. [38], where pressure fluctuation is given by

$$\frac{1}{\rho}\frac{\partial^2 p'}{\partial x_i \partial x_i} = -\frac{\partial u_i}{\partial x_j}\frac{\partial u_j}{\partial x_i}, \tag{3}$$

with pressure boundary condition given by

$$\frac{1}{\rho}\left.\frac{\partial p'}{\partial x_2}\right|_{x_2=0,2h} = \nu\frac{\partial^2 u_2}{\partial x_i \partial x_i} - \frac{\partial u_2}{\partial t}. \tag{4}$$

III. Results and Discussion

A. Turbulent drag response under RPM-based subsurface metamaterial surface

We first investigate the turbulent drag response under the RPM-based metamaterial surface, as shown in Fig. 3. The figure compares the temporal evolution of the relative wall shear stress, $\tau_w/\bar{\tau}_{w,0}$, between the RPM-controlled flow and a prescribed blowing and suction case, where $(\bar{\cdot})$ indicates a temporal average. The prescribed case is designed to have a comparable wall-normal velocity amplitude to that produced by the RPM subsurface when averaged over a selected time horizon. The wall transpiration profile for the prescribed control is given by

$$u_2|_{x_2=0} = A\cos(\kappa_1 x_1)\cos(\omega t), \tag{5}$$

where κ_1 is the streamwise wave number. However, in the subsequent analysis, it is observed that the oscillation amplitude of the RPM-based surface for the chosen case C2A4 is not stationary and continues to decay gradually over time. Consequently, the corresponding variation in turbulent drag cannot be strictly regarded as a statistically steady response.

Over the control horizon $t^+ \in (0, 4000)$, the mean drag of the RPM subsurface case (Fig. 3a) remains lower than that of the prescribed control (Fig. 3b) with a similar effective amplitude. The passive RPM configuration achieves a drag reduction of approximately $\%\Delta\tau_w = -1.34$, whereas the prescribed forcing yields a larger reduction of $\%\Delta\tau_w = -2.31$. However, the stronger drag reduction achieved by the prescribed control is accompanied by a pronounced increase in instantaneous shear-stress fluctuations. In contrast, the RPM subsurface, owing to its dynamic and passive nature, maintains smoother temporal variations in wall shear stress. The maximum drag is suppressed under the uncontrolled

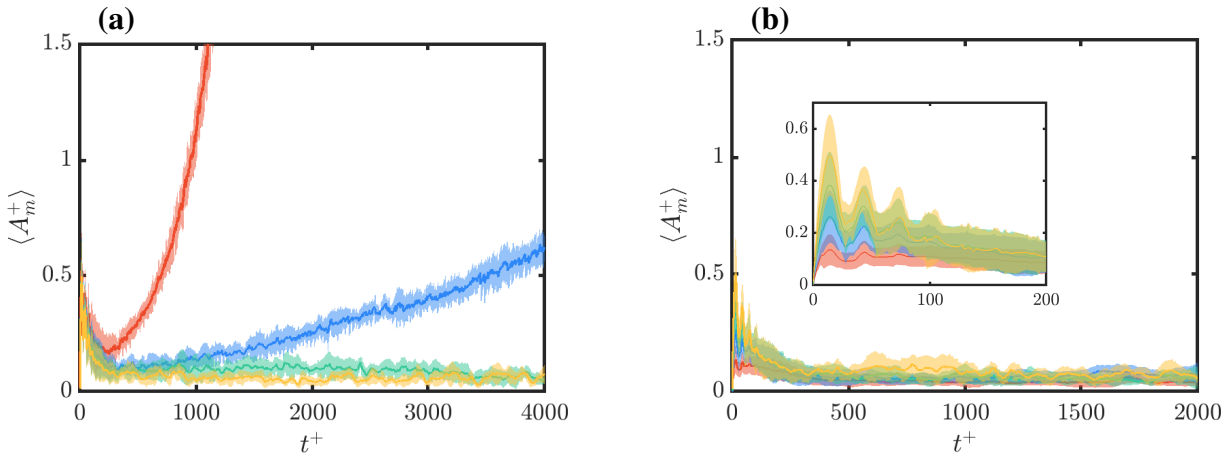

Fig. 4 Time evolution of peak-to-peak actuation velocity amplitude $\langle A_m^+ \rangle$ for cases with varying damping coefficients $\tilde{c}$ (C1A4, red; C2A4, blue; C3A4, green; C4A4, yellow) (a) and mass and stiffness constants ($\tilde{m}_{\text{def}}, \tilde{k}_{\text{g,def}}$) (C3A1, red; C3A2, blue; C3A3, green; C3A4, yellow) (b). Inset shows early-time transient response. Solid line denotes the mean across different control panels, and the shaded area denotes the standard deviation.

flow, while the prescribed case has significantly higher drag at its maximum. This highlights a fundamental trade-off: while active or prescribed controls can achieve higher mean drag reduction, the passive RPM subsurface offers improved stability and robustness by avoiding large-amplitude oscillations in friction velocity.

B. Fluid-metamaterial interaction

To further understand the coupled dynamics between the turbulent flow and the RPM-based subsurface, we investigate the temporal evolution of the wall-normal actuation velocity amplitude $\langle A_m^+ \rangle$ under different RPM configurations, where $\langle \cdot \rangle$ denotes an average over each panel. Figure 4(a) illustrates the time evolution of the peak-to-peak wall-normal actuation velocity $\langle A_m^+ \rangle$ for varying damping coefficients $\tilde{c}$, while the mass and stiffness constants are fixed. The peak-to peak velocity A_m is defined as the local maxima of oscillating velocity amplitude for the control panels. A clear bifurcation behavior is observed with respect to the damping coefficient. For $\tilde{c} < 0.48$ (cases C1A4 and C2A4), the oscillation amplitude grows continuously with time, indicating an unstable regime where the compliant surface motion amplifies under the influence of the turbulent forcing. In contrast, for $\tilde{c} > 0.51$ (cases C3A4 and C4A4), the oscillation amplitude remains bounded and gradually converges to a steady state with $\langle A_m^+ \rangle \approx 0.1$. These results suggest that the critical damping coefficient $\tilde{c}_{\text{crit}}$ separating the stable and unstable regimes lies between $\tilde{c} = 0.48$ and 0.51.

Figure 4(b) presents the evolution of peak-to-peak actuation velocity amplitude $\langle A_m^+ \rangle$ for cases with varying mass and stiffness parameters ($\tilde{m}_{\text{def}}, \tilde{k}_{g,\text{def}}$) at a fixed damping coefficient $\tilde{c} = 0.51$. All cases converge to a similar steady-state amplitude around $\langle A_m^+ \rangle \approx 0.1$, demonstrating that the equilibrium response amplitude is largely independent of the mass and stiffness configuration for the system in the overdamped regime ($\tilde{c} > \tilde{c}_{\text{crit}}$).

This bifurcation behavior has direct implications for the achievable drag reduction performance. As shown by Lin et al. [8], there exists an optimal range of wall-transpiration amplitude, approximately $\langle A_m^+ \rangle \approx 0.7$, that yields maximum drag reduction in sinusoidal wall-forcing studies. When the oscillation amplitude falls below this range, the drag reduction effect diminishes significantly. Therefore, while the overdamped RPM configurations offer stability and robustness, they also limit the attainable wall-normal velocity amplitude, thereby constraining the potential for substantial drag reduction. Therefore, achieving a higher steady-state response through appropriate combinations of RPM parameters represents a potential pathway toward enhanced drag reduction using phononic metamaterials.

To further reveal the coupled dynamics between the turbulent flow and the RPM-based subsurface, we evaluate the spectrograms of the input forcing and the corresponding output response for each control panel. The spectrogram of a generic time-dependent quantity $\mathcal{X}(t)$ is defined as

$$S_{\mathcal{X}}(t, \omega) = \int_t^{t+\Delta t} \mathcal{X}(\tau)\, e^{-i\omega\tau}\, d\tau, \tag{6}$$

where Δt denotes the minimal temporal window required to resolve the dominant frequency content of $\mathcal{X}$. The

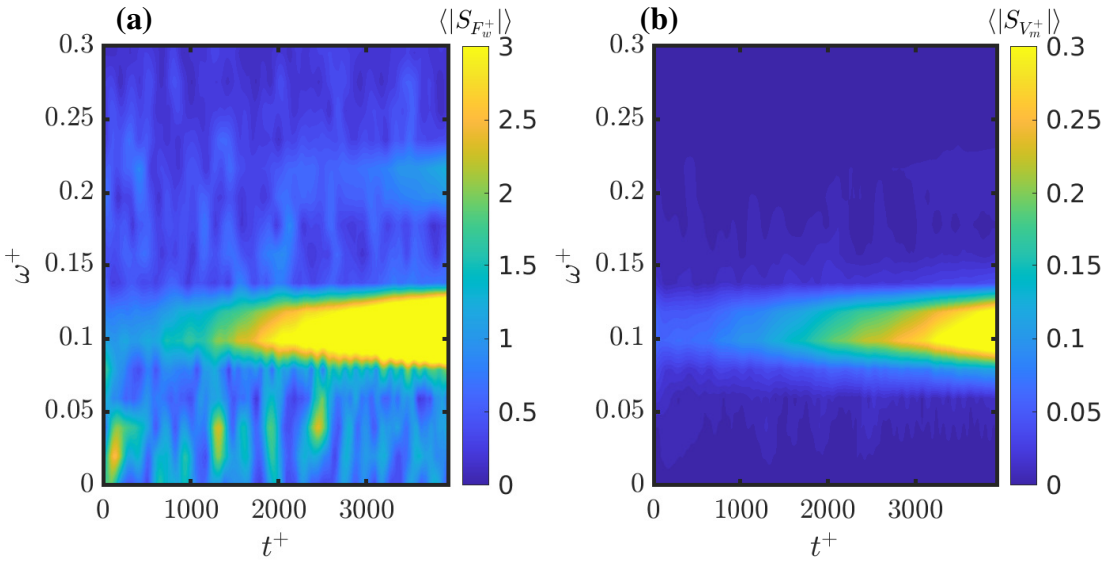

Fig. 5 Spectrogram of panel-averaged magnitude of the wall-normal force $\langle|S_{F_w^+}|\rangle$ (a) and peak velocity $\langle|S_{V_m^+}|\rangle$ (b) for case C2A4 computed using a time window of $\Delta t^+ \approx 300$.

spectrograms enable us to capture the time-varying frequency content by averaging over a relatively short time horizon of $\Delta t^+ \approx 300$. Figure 5 presents the time-resolved spectrograms of the wall-normal load, $\langle|S_{F_w^+}|\rangle$, and the corresponding surface response velocity, $\langle|S_{V_m^+}|\rangle$ averaged over control panels, for the representative critical case C2A4.

In Fig. 5(b), the spectrogram of the wall-normal velocity response shows that the RPM surface oscillates predominantly around a single frequency, $\omega^+ \approx 0.11$. This dominant frequency coincides with the pre-designed value obtained from the linear response analysis of the RPM model. This agreement confirms that the designed RPM configuration is capable of producing a stable, single-frequency oscillation even under broadband turbulent wall-pressure excitation, as evidenced by the forcing spectrogram shown in Fig. 5 (a). Moreover, the wall-normal load spectrogram, $\langle|S_{F_w^+}|\rangle$, is also centered around the same frequency band, indicating a strong flow-structure coupling near the design frequency. The alignment of the forcing and response spectra suggests that the compliant metamaterial subsurface behaves as a resonant oscillator with the turbulent flow under a critical damping coefficient. This mechanism explains the onset of instability observed in configurations with low damping ($\tilde{c} < \tilde{c}_{\text{crit}}$), where the resonant interaction between the turbulent flow and the compliant subsurface leads to growing unstable oscillation amplitude.

On the other hand, Fig. 6 illustrates the spectrogram for a high damping FSI configuration, C3A4, which exhibits a distinctly different mechanism. The velocity spectrum still shows that the dominant frequency remains aligned with the designed forcing frequency, with a similar level of dispersion as observed in the low damping configuration (e.g., C2A4). However, the wall-normal load spectrogram responds with a relatively weak oscillation at the forcing frequency. We attribute this behavior to the sufficiently large damping coefficient, which acts as an energy sink that extracts near-wall turbulent energy, thereby suppressing the growth of wall-normal load through the resonant amplification mechanism present in the underdamped system.

C. Linear model of wall pressure

In the previous section, we identified that the critical damping coefficient lies between $\tilde{c} = 0.48$ and $\tilde{c} = 0.51$. However, this bifurcation threshold is only valid for the current set of RPM parameters and the specific control panel configuration. Since each simulation requires substantial computational resources to perform DNS of turbulent flow, it becomes essential to develop a surrogate model to capture the coupled dynamic between turbulent flow and RPM model. To be more specific, we would like to propose a reduced-order model (ROM) for wall pressure that can effectively replace the full Navier–Stokes equations within the weakly coupled framework. In this section, we introduce a linearized model based solely on wall quantities, providing a fast yet accurate predictive tool for future design and optimization of RPM-based compliant surfaces.

Before constructing the reduced-order model, it is necessary to examine the relative contributions of the mean pressure gradient, $\bar{p}$, and the pressure fluctuation, p'. By integrating over each control panel, the input wall-normal

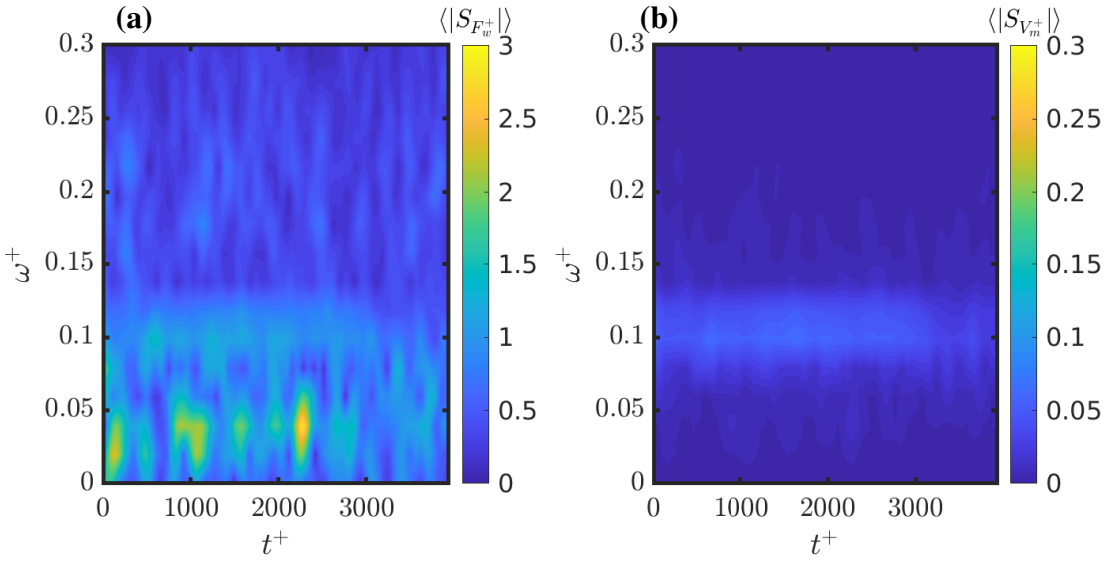

Fig. 6 Spectrogram of panel-averaged magnitude of the wall-normal force $\langle|S_{F_w^+}|\rangle$ (a) and peak velocity $\langle|S_{V_m^+}|\rangle$ (b) for case C3A4 computed using a time window of $\Delta t^+ \approx 300$.

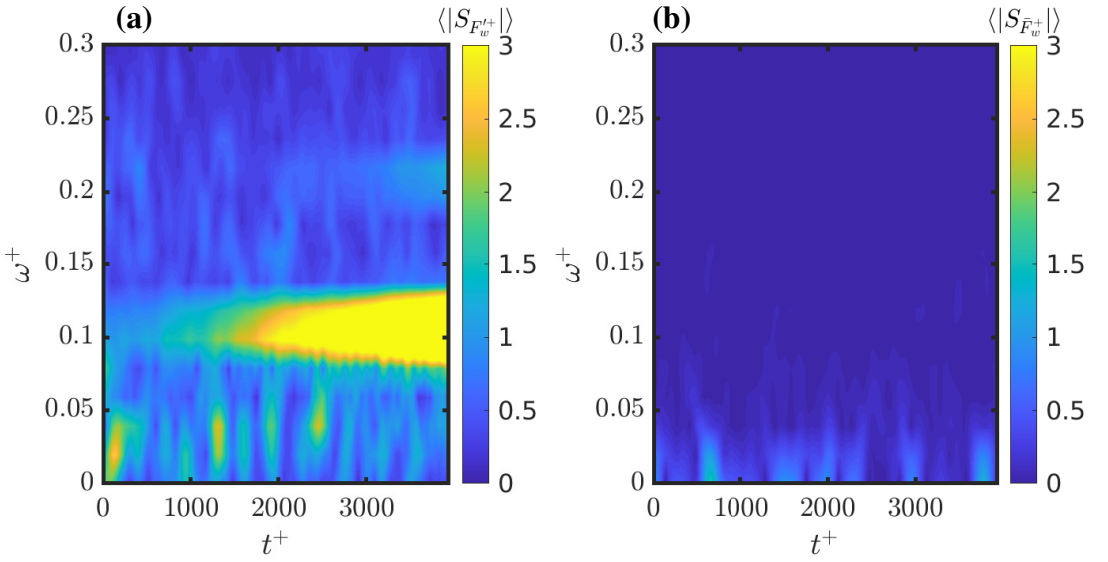

Fig. 7 Spectrogram of panel-averaged magnitude of the fluctuating force $\langle|S_{F_w'^+}|\rangle$ (a) and mean wall-normal force $\langle|S_{\bar{F}_w^+}|\rangle$ (b) for case C2A4 computed using a time window of $\Delta t^+ \approx 300$.

load can be decomposed into the mean component, $\bar{F}_w$, and the fluctuating component, F'_w. Comparing Fig. 7 with Fig. 5, this decomposition reveals that the dominant contribution to the wall-normal forcing originates from the pressure fluctuation field. The mean pressure gradient primarily contributes to the low-frequency content, while the fluctuation component governs the resonant dynamics at the forcing frequency. Therefore, the main focus of the following analysis is to model the pressure fluctuation using only information available from the wall boundary conditions.

The pressure Poisson equation can be written as

$$\frac{1}{\rho}\frac{\partial^2 p}{\partial x_i \partial x_i} = \frac{\partial}{\partial x_i}\left(\nu\frac{\partial^2 u_i}{\partial x_j \partial x_j} - u_j\frac{\partial u_i}{\partial x_j}\right) = -\frac{\partial u_i}{\partial x_j}\frac{\partial u_j}{\partial x_i} = f_{f,s}, \tag{7}$$

where $f_{f,s}$ denotes the source term, comprising the conventionally defined fast and slow contributions to the pressure field. The corresponding boundary conditions at the walls are expressed as

$$P_b \equiv \frac{1}{\rho}\left.\frac{\partial p}{\partial x_2}\right|_{x_2=0} = \left.\left(\nu\frac{\partial^2 u_2}{\partial x_j \partial x_j} - \frac{\partial u_2}{\partial t}\right)\right|_{x_2=0}, \tag{8}$$

$$P_t \equiv \frac{1}{\rho}\left.\frac{\partial p}{\partial x_2}\right|_{x_2=2h} = \left.\left(\nu\frac{\partial^2 u_2}{\partial x_j \partial x_j} - \frac{\partial u_2}{\partial t}\right)\right|_{x_2=2h}. \tag{9}$$

From previous studies [38, 39], it has been shown that the equation 7 with the boundary conditions can be solved analytically via the Fourier transform in the streamwise and spanwise direction. The solution can then be expressed as the sum of inhomogeneous and homogeneous components,

$$\hat{p}' = \underbrace{\hat{p}_{f,s}}_{\text{inhomogenoeus}} + \underbrace{\hat{p}_{st}}_{\text{homogeneous}}, \tag{10}$$

where $\hat{(\cdot)}$ is the Fourier transform in the streamwise and spanwise directions. The inhomogeneous solution $\hat{p}_{f,s}$ is obtained via the Green's function,

$$G(x_2, x_2', \kappa \neq 0) = \begin{cases} \dfrac{\cosh[\kappa(x_2'/h - 2)]\cosh[\kappa(x_2/h)]}{\kappa\sinh(2\kappa)}, & \text{for } x_2 < x_2', \\ \dfrac{\cosh[\kappa(x_2'/h)]\cosh[\kappa(x_2/h - 2)]}{\kappa\sinh(2\kappa)}, & \text{for } x_2 > x_2', \end{cases} \tag{11}$$

$$G(x_2, x_2', \kappa = 0) = \begin{cases} 0.5(x_2' - x_2)/h, & x_2 < x_2', \\ 0.5(x_2 - x_2')/h, & x_2 > x_2', \end{cases}$$

as

$$\hat{p}_{f,s}(x_2, \kappa) = \int_0^{2h} G(x_2, x_2', \kappa)\, \hat{f}_{f,s}(x_2', \kappa)\, \mathrm{d}x_2', \tag{12}$$

where $\kappa = \sqrt{\kappa_1^2 + \kappa_3^2}$, and κ_1 and κ_3 are streamwise and spanwise wavenumbers, respectively. The homogeneous solution $\hat{p}_{st}$ is given by

$$\hat{p}_{st}(x_2, \kappa) = \frac{1}{\kappa\sinh(2\kappa)}\left(\hat{P}_t\cosh[\kappa x_2] - \hat{P}_b\cosh[\kappa(x_2 - 2h)]\right). \tag{13}$$

To establish a computationally efficient framework for simulating pressure fluctuations, we employ a linearized formulation derived from the pressure Poisson equation. Here, we adopt the hypothesis that only the near-wall events will affect the wall pressure. Although turbulence is inherently nonlocal and nonlinear, numerous studies have demonstrated that certain linear mechanisms persist within fully turbulent flows [39, 40].

Focusing on the near-wall region, the right-hand side of the pressure Poisson equation can be approximated by the dominant term $(\partial u_1/\partial x_2)(\partial u_2/\partial x_1)$. At the boundary, the streamwise derivative of wall-normal velocity is known due to the imposed blowing and suction distribution, while the wall-normal gradient of the streamwise velocity can be approximated as constant based on the law of the wall,

$$u_1^+ \approx x_2^+ \quad \Rightarrow \quad \frac{\partial u_1}{\partial x_2} \approx \frac{u_{\tau,o}^2}{\nu}, \tag{14}$$

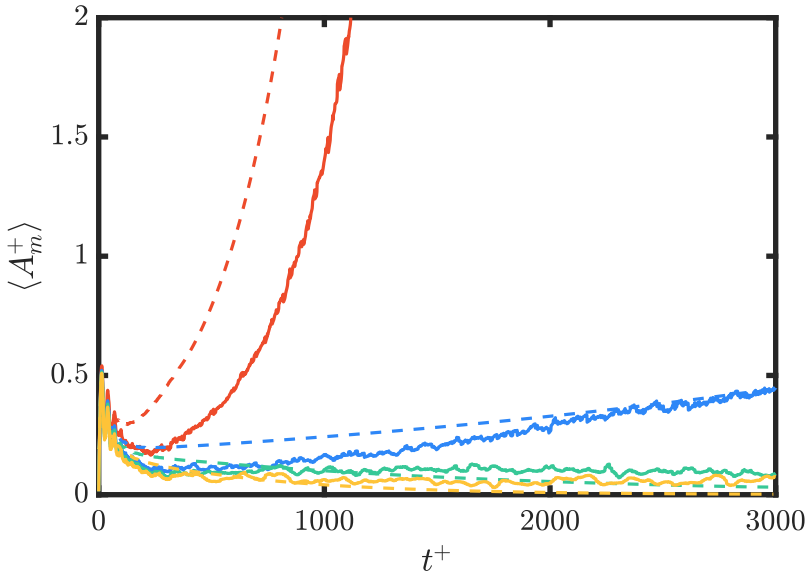

Fig. 8 Time evolution of the peak-to-peak wall-normal actuation velocity amplitude, $\langle A_m^+ \rangle$, for different control configurations from DNS (solid lines) and the current ROM with $\nu_c/\nu = 0.295$ (dashed lines) for C1A4, red; C2A4, blue; C3A4, green; C4A4, yellow.

where $u_{\tau,o}$ is the friction velocity of uncontrolled flow. Restricting the integration to the viscous sublayer, the inhomogeneous pressure contribution at the wall ($x_2 = 0$) can be approximated as

$$\hat{p}_{f,s}(x_2 = 0, \kappa) \approx \int_0^{\delta_2} G(x_2 = 0, x_2', \kappa)\, \hat{f}_{f,s}(x_2', \kappa)\, \mathrm{d}x_2' \approx -2 \int_0^{\delta_2} G(x_2 = 0, x_2', \kappa) \frac{\partial u_1}{\partial x_2} \frac{\partial \hat{u}_2}{\partial x_1}\bigg|_{x_2=0} \mathrm{d}x_2', \tag{15}$$

where δ_2 denotes the sublayer region, set to $\delta_2^+ = 0.1$ in this study.

The homogeneous component can be further simplified using the boundary condition. Although the blowing and suction profile of the RPM-based control panel varies in the streamwise direction, the viscous term $\nu\partial^2 u_2/(\partial x_1)^2$ is much smaller than the wall-normal gradient term and can therefore be neglected. Furthermore, the viscous term is modeled as proportional to the unsteady term,

$$\nu \frac{\partial^2 u_2}{\partial x_2^2} \approx \left(1 - \frac{\nu_c}{\nu}\right) \frac{\partial u_2}{\partial t}, \tag{16}$$

where ν_c denotes a proportional coefficient capturing the damping effect of the wall. The boundary condition is thus modeled as

$$P_b \approx \nu \frac{\partial^2 u_2}{\partial x_2^2} - \frac{\partial u_2}{\partial t}\bigg|_{x_2=0} \approx -\frac{\nu_c}{\nu} \frac{\partial u_2}{\partial t}\bigg|_{x_2=0}, \quad P_t = 0. \tag{17}$$

Here, we set $\nu_c/\nu = 0.295$. The value of this hyperparameter is determined from the relative scaling between the unsteady term and the viscous term appearing in the boundary-condition approximation. Combining the expressions yields the simplified homogeneous solutions estimate close to the bottom wall, we get

$$\hat{p}_{st}(x_2 = 0, \kappa) = \frac{1}{\kappa \sinh(2\kappa)} \left(-\frac{\nu_c}{\nu} \frac{\partial \hat{u}_2}{\partial t}\bigg|_{x_2=0} \cosh(-2\kappa h) \right). \tag{18}$$

With both the simplified inhomogeneous and homogeneous solutions, the wall pressure at each time step can be obtained directly from the prescribed wall-normal blowing and suction,

$$\hat{p}'|_{x_2=0} = -2 \int_0^{\delta_2} G(x_2 = 0, x_2', \kappa) \frac{u_{\tau,o}^2}{\nu} \frac{\partial \hat{u}_2}{\partial x_1}\bigg|_{x_2=0} \mathrm{d}x_2' + \frac{1}{\kappa \sinh(2\kappa)} \left(-\frac{\nu_c}{\nu} \frac{\partial \hat{u}_2}{\partial t}\bigg|_{x_2=0} \cosh(-2\kappa h) \right). \tag{19}$$

Given this wall pressure, the weakly-coupled scheme can then be closed. To validate the ROM, Fig. 8 presents the model predictions for various damping coefficients. In the figure, the dashed lines denote the predictions obtained from the reduced-order model, while the solid lines represent the DNS results with identical RPM parameter settings. By selecting a constant value of $\nu_c/\nu = 0.295$, the model successfully captures the major bifurcation behavior within the critical damping range. However, it is worth noting that for the underdamped case C1A4, the model reproduces the unstable dynamics but over a different time scale, exhibiting a tendency to overpredict the instability amplitude. These results suggest that the proportional parameter ν_c/ν may depend on the RPM parameters or the near-wall flow characteristics. Further investigation is therefore required to establish this relationship and to complete the development of a robust surrogate model for the weakly coupled pressure–compliant wall system.

IV. Conclusion

In this study, we investigated the interaction between resonant phononic materials (RPMs) and a turbulent channel flow using a weakly coupled fluid-metamaterial interaction (FMI) framework. By designing the metamaterial subsurface to exhibit a defect-induced resonance matched to the dominant frequency–wavelength pairs identified in prior active-control studies, we demonstrated that the compliant RPM interface can passively convert broadband near-wall turbulence into a single-frequency oscillatory wall motion.

Our DNS results reveal that the response of the RPM-flow system depends sensitively on the damping coefficient. A clear bifurcation separates an underdamped regime, in which resonant coupling induces growing oscillatory amplitude, from an overdamped regime characterized by bounded surface motion. Configurations near this critical damping threshold yield non-negligible transient drag reduction ($\%\Delta\tau_w \approx 1.34$), enabled by the collapse of the wall-normal forcing and RPM response onto a narrow frequency band centered at the designed defect resonance. Notably, this drag reduction is achieved without the large shear-stress excursions observed in equivalent prescribed-forcing cases, indicating that the compliant subsurface offers enhanced robustness and stability despite lower peak drag-reduction levels.

To enable rapid exploration of RPM parameter space, we developed a reduced-order wall-pressure model based on a linearized form of the pressure Poisson equation and a near-wall approximation of its source terms. The resulting surrogate model captures the primary bifurcation behavior and reproduces the qualitative growth or saturation trends across the damping-parameter sweep. While discrepancies persist in the unstable regime, suggesting that the proportional parameter ν_c depends on local flow or structural properties, the model provides a promising foundation for fast predictive design of compliant-wall systems.

Overall, this study demonstrates that resonant phononic subsurfaces offer a viable pathway toward passive, dynamically adaptive drag reduction in turbulent flows. Future work will focus on extending the present weakly coupled framework to strongly coupled FSI, exploring practically realizable RPM architectures, and refining the reduced-order model through a parameterized, physics-informed prediction of the proportional coefficient ν_c/ν.

Acknowledgments

This work is supported by AFOSR MURI under grant number FA9550-23-1-0299.

References

[1] Kornilov, V., "Combined Blowing/Suction Flow Control on Low-Speed Airfoils," *Flow, Turbulence and Combustion*, Vol. 106, 2021. https://doi.org/10.1007/s10494-020-00157-7.

[2] Kushwaha, M. S., Halevi, P., Dobrzynski, L., and Djafari-Rouhani, B., "Acoustic band structure of periodic elastic composites," *Physical Review Letters*, Vol. 71, 1993, pp. 2022–2025. https://doi.org/10.1103/PhysRevLett.71.2022, URL https://link.aps.org/doi/10.1103/PhysRevLett.71.2022.

[3] Ramakrishnan, V., and Frazier, M. J., "Architected material with independently tunable mass, damping, and stiffness via multi-stability and kinematic amplification," *The Journal of the Acoustical Society of America.*, Vol. 153, No. 2, 2023, pp. 1283–1292. https://doi.org/10.1121/10.0017346, URL https://doi.org/10.1121/10.0017346.

[4] Lu, Y., and Park, H. S., "Double Dirac cones and topologically nontrivial phonons for continuous square symmetric $C_{4(v)}$ and $C_{2(v)}$ unit cells," *Physics Review B*, Vol. 103, 2021, p. 064308. https://doi.org/10.1103/PhysRevB.103.064308, URL https://link.aps.org/doi/10.1103/PhysRevB.103.064308.

[5] Chen, Y., Wen, X., Lu, Y., Lan, Z., Fan, L., Park, H. S., Gu, Z., Zhu, J., and Su, Z., "Broadband large-scale acoustic topological waveguides," *Composite Structures*, Vol. 352, 2025, p. 118669. https://doi.org/10.1016/j.compstruct.2024.118669, URL https://doi.org/10.1016/j.compstruct.2024.118669.

[6] Neville, R. M., Scarpa, F., and Pirrera, A., "Shape morphing Kirigami mechanical metamaterials," *Scientific reports*, Vol. 6, No. 1, 2016, p. 31067. URL https://doi.org/10.1038/srep31067.

[7] Xu, R., Chen, C., Sun, J., He, Y., Li, X., Lu, M.-H., and Chen, Y., "The design, manufacture and application of multistable mechanical metamaterials-a state-of-the-art review," *International Journal of Extreme Manufacturing*, Vol. 5, No. 4, 2023, p. 042013. https://doi.org/10.1088/2631-7990/acf96a, URL https://iopscience.iop.org/article/10.1088/2631-7990/acf96a/meta.

[8] Lin, C.-T., Goza, A., and Bae, H. J., "Active control for turbulent drag reduction by periodic blowing and suction," *AIAA AVIATION FORUM AND ASCEND 2024*, 2024, p. 3636. https://doi.org/10.2514/6.2024-3636.

[9] Kramer, M., "Boundary-layer stabilization by distributed damping," *Journal of the Aeronautical Sciences*, Vol. 24, No. 6, 1957, pp. 459–460.

[10] Kramer, M. O., "Boundary-Layer Stabilization by Distributed Damping," *Journal of the Aerospace Sciences*, Vol. 27, No. 1, 1960, pp. 69–69. https://doi.org/10.2514/8.8380, URL https://doi.org/10.2514/8.8380.

[11] Kramer, M. O., "Boundary layer stabilization by distributed damping," *Naval Engineers Journal*, Vol. 74, 1962, pp. 341–348. URL https://api.semanticscholar.org/CorpusID:111249163.

[12] Carpenter, P. W., and Garrad, A. D., "The hydrodynamic stability of flow over Kramer-type compliant surfaces. Part 1. Tollmien-Schlichting instabilities," *Journal of Fluid Mechanics*, Vol. 155, 1985, p. 465–510. https://doi.org/10.1017/S0022112085001902.

[13] Carpenter, P. W., and Garrad, A. D., "The hydrodynamic stability of flow over Kramer-type compliant surfaces. Part 2. Flow-induced surface instabilities," *Journal of Fluid Mechanics*, Vol. 170, 1986, p. 199–232. https://doi.org/10.1017/S002211208600085X.

[14] Davies, C., and Carpenter, P. W., "Instabilities in a plane channel flow between compliant walls," *Journal of Fluid Mechanics*, Vol. 352, 1997, p. 205–243. https://doi.org/10.1017/S0022112097007313.

[15] Davies, C., and Carpenter, P. W., "Numerical simulation of the evolution of Tollmien–Schlichting waves over finite compliant panels," *Journal of Fluid Mechanics*, Vol. 335, 1997, p. 361–392. https://doi.org/10.1017/S0022112096004636.

[16] Wang, Z., Yeo, K. S., and Khoo, B. C., "Spatial direct numerical simulation of transitional boundary layer over compliant surfaces," *Computers & Fluids*, Vol. 34, 2005, pp. 1062–1095. URL https://api.semanticscholar.org/CorpusID:121675415.

[17] Wang, Z., Yeo, K., and Khoo, B., "On two-dimensional linear waves in Blasius boundary layer over viscoelastic layers," *European Journal of Mechanics - B/Fluids*, Vol. 25, No. 1, 2006, pp. 33–58. https://doi.org/https://doi.org/10.1016/j.euromechflu.2005.04.006, URL https://www.sciencedirect.com/science/article/pii/S0997754605000488.

[18] Hussein, M. I., Biringen, S., Bilal, O. R., and Kucala, A., "Flow stabilization by subsurface phonons," *Proceedings of the Royal Society A: Mathematical, Physical and Engineering Sciences*, Vol. 471, No. 2177, 2015, p. 20140928. https://doi.org/10.1098/rspa.2014.0928, URL https://royalsocietypublishing.org/doi/abs/10.1098/rspa.2014.0928.

[19] Barnes, C. J., Willey, C. L., Rosenberg, K., Medina, A., and Juhl, A. T., "Initial computational investigation toward passive transition delay using a phononic subsurface," *AIAA Scitech 2021 Forum*, 2021, p. 1454. https://doi.org/10.2514/6.2021-1454, URL https://arc.aiaa.org/doi/abs/10.2514/6.2021-1454.

[20] Willey, C. L., Barnes, C. J., Chen, V. W., Rosenberg, K., Medina, A., and Juhl, A. T., "Multi-input multi-output phononic subsurfaces for passive boundary layer transition delay," *Journal of Fluids and Structures*, Vol. 121, 2023, p. 103936. https://doi.org/https://doi.org/10.1016/j.jfluidstructs.2023.103936, URL https://www.sciencedirect.com/science/article/pii/S0889974623001044.

[21] Bushnell, D. M., Hefner, J. N., and Ash, R. L., "Effect of compliant wall motion on turbulent boundary layers," *The Physics of Fluids*, Vol. 20, No. 10, 1977, pp. S31–S48. https://doi.org/10.1063/1.861756, URL https://doi.org/10.1063/1.861756.

[22] Duncan, J. H., "The response of an incompressible, viscoelastic coating to pressure fluctuations in a turbulent boundary layer," *Journal of Fluid Mechanics*, Vol. 171, 1986, p. 339–363. https://doi.org/10.1017/S0022112086001477.

[23] Kireiko, G. V., "Interaction of wall turbulence with a compliant surface," *Fluid Dynamics*, Vol. 25, No. 4, 1990, pp. 550–554. https://doi.org/10.1007/BF01049861, URL https://doi.org/10.1007/BF01049861.

[24] Endo, T., and Himeno, R., "Direct numerical simulation of turbulent flow over a compliant surface," *Journal of Turbulence*, Vol. 3, 2002, p. N7. https://doi.org/10.1088/1468-5248/3/1/007, URL https://doi.org/10.1088/1468-5248/3/1/007.

[25] Fukagata, K., Kern, S., Chatelain, P., Koumoutsakos, P., and Kasagi, N., "Evolutionary optimization of an anisotropic compliant surface for turbulent friction drag reduction," *Journal of Turbulence*, Vol. 9, 2008, p. N35. https://doi.org/10.1080/14685240802441126, URL https://doi.org/10.1080/14685240802441126.

[26] Józsa, T. I., Balaras, E., Kashtalyan, M., Borthwick, A. G. L., and Viola, I. M., "Active and passive in-plane wall fluctuations in turbulent channel flows," *Journal of Fluid Mechanics*, Vol. 866, 2019, p. 689–720. https://doi.org/10.1017/jfm.2019.145.

[27] Kim, E., and Choi, H., "Space–time characteristics of a compliant wall in a turbulent channel flow," *Journal of Fluid Mechanics*, Vol. 756, 2014, p. 30–53. https://doi.org/10.1017/jfm.2014.444.

[28] Luhar, M., Sharma, A., and McKeon, B., "A framework for studying the effect of compliant surfaces on wall turbulence," *Journal of Fluid Mechanics*, Vol. 768, 2015, p. 415–441. https://doi.org/10.1017/jfm.2015.85.

[29] Quadrio, M., Floryan, J. M., and Luchini, P., "Effect of streamwise-periodic wall transpiration on turbulent friction drag," *Journal of Fluid Mechanics*, Vol. 576, 2007, p. 425–444. https://doi.org/10.1017/S0022112007004727.

[30] Ramakrishnan, V., and Matlack, K. H., "A quantitative study of energy localization characteristics in defect-embedded monoatomic phononic crystals," *Journal of Sound and Vibration*, Vol. 614, 2025, p. 119164. https://doi.org/https://doi.org/10.1016/j.jsv.2025.119164, URL https://www.sciencedirect.com/science/article/pii/S0022460X2500238X.

[31] Deymier, P. A., Ed., *Acoustic Metamaterials and Phononic Crystals*, Heidelberg: Springer, 2013. URL https://link.springer.com/book/10.1007/978-3-642-31232-8.

[32] Orlandi, P., *Fluid flow phenomena: a numerical toolkit*, Vol. 55, Springer Science & Business Media, 2000. URL https://link.springer.com/book/10.1007/978-94-011-4281-6.

[33] Kim, J., and Moin, P., "Application of a fractional-step method to incompressible Navier-Stokes equations," *Journal of Computational Physics*, Vol. 59, No. 2, 1985, pp. 308–323. https://doi.org/https://doi.org/10.1016/0021-9991(85)90148-2.

[34] Wray, A. A., "Minimal storage time advancement schemes for spectral methods," *NASA Ames Research Center, California, Report No. MS*, Vol. 202, 1990. URL https://www.researchgate.net/publication/246830945_Minimal_storage_time-advancement_schemes_for_spectral_methods.

[35] Bae, H. J., Lozano-Durán, A., Bose, S. T., and Moin, P., "Turbulence intensities in large-eddy simulation of wall-bounded flows," *Physics Review Fluids*, Vol. 3, 2018, p. 014610. https://doi.org/10.1103/PhysRevFluids.3.014610.

[36] Bae, H. J., Lozano-Durán, A., Bose, S. T., and Moin, P., "Dynamic slip wall model for large-eddy simulation," *Journal of Fluid Mechanics*, Vol. 859, 2019, p. 400–432. https://doi.org/10.1017/jfm.2018.838.

[37] Lozano-Duran, A., and Bae, H. J., "Turbulent channel with slip boundaries as a benchmark for subgrid-scale models in LES," *Annual research briefs. Center for Turbulence Research*, Vol. 2016, 2016, pp. 97–103. URL https://pmc.ncbi.nlm.nih.gov/articles/PMC6800701/.

[38] Toedtli, S., Leonard, A., and McKeon, B., "Coupled dynamics of wall pressure and transpiration, with implications for the modelling of tailored surfaces and turbulent drag reduction," *Journal of Fluid Mechanics*, Vol. 1019, 2025, p. A18. https://doi.org/10.1017/jfm.2025.10532.

[39] Kim, J., "On the structure of pressure fluctuations in simulated turbulent channel flow," *Journal of Fluid Mechanics*, Vol. 205, 1989, p. 421–451. https://doi.org/10.1017/S0022112089002090.

[40] Jiménez, J., "Near-wall turbulence," *Physics of Fluids*, Vol. 25, No. 10, 2013, p. 101302. https://doi.org/10.1063/1.4824988, URL https://doi.org/10.1063/1.4824988.